

In Situ Fluorescence Imaging of Oxygen Evolution on Epitaxial Perovskite Films with Composition Gradients

Daniel J. Zheng, Haldrian Iriawan, Rohit Pant, C. John Eom, Hongbin Xu, Jiayu Peng, Cat Arase, Ichiro Takeuchi, Yuriy Román-Leshkov, and Yang Shao-Horn*



Cite This: *ACS Catal.* 2025, 15, 8776–8787



Read Online

ACCESS |



Metrics & More

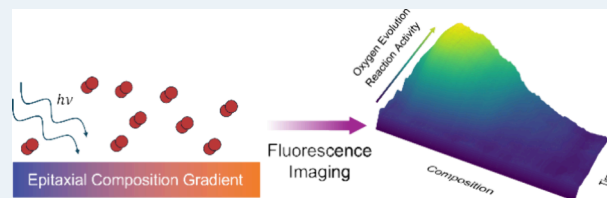


Article Recommendations



Supporting Information

ABSTRACT: The oxygen evolution reaction (OER) is critical for the efficient electrochemical conversion of earth-abundant molecules and materials into more useful energy carriers, fuels, and value-added commodities. However, the sluggish kinetics of the OER leads to high overpotentials needed to catalyze the reaction, despite significant efforts to rationally design highly active OER catalysts. To date, most OER catalyst discovery has relied on human-driven approaches that have led to an understanding of only a small proportion of all possible materials. In recent years, the advent of high-throughput virtual screening and machine learning has significantly increased the space that has been explored, but methods for experimentally validating the OER activities at scale are still limited and challenging. In this work, we report a fluorescence-based high-throughput screening method for OER catalysts. We detailed a simple, custom-built cell with a fluorescent detector that changed colors upon O₂ contact to screen the La_{0.6}Sr_{0.4}Fe_xCo_{1-x}O₃ composition space. Using kinetic measurements of the fluorescence evolution as a function of the O₂ evolved, apparent OER rates for the entire composition space were extracted, which revealed that $x = 0.20 \pm 0.05$ appears to be the most active within the chemical space. Density functional theory calculations revealed a decrease in the computed OER overpotential on both Co and Fe sites of La_{0.5}Sr_{0.5}Fe_xCo_{1-x}O₃ (001) with increasing Co doping, where $x = 0.25$ was found to be the most active, hence validating the observed trend and demonstrating the validity of the setup for screening the entire composition space simultaneously.



KEYWORDS: oxygen evolution, high-throughput, fluorescence, perovskites, epitaxial, computation

INTRODUCTION

Production of hydrogen-based energy carriers is critical to facilitate the decarbonization of the energy supply chain and transition away from nonrenewable energy sources. The electrocatalysis of the oxygen evolution reaction (OER) is central to the conversion of molecules and materials in equilibrium at ambient conditions into carbon-neutral or free energy carriers or fuels, such as the electrochemical splitting of H₂O to H₂ and the electro-conversion of CO₂ into hydrocarbon-based fuels.¹ However, state-of-the-art OER catalysts require high overpotentials to enable current densities needed for practical applications,^{2,3} which severely limits the efficiency of these electrochemical devices. For example, the reaction overpotential from the OER in alkaline electrolyzers constitutes over 60% of the losses at current densities of ~1 A cm⁻².^{1,4} Significant efforts have already been invested in studying classic OER catalysts to increase their activity further such as studying the OER mechanism and rates on different sites of single-crystal RuO₂^{5,6} and IrO₂⁷ surfaces. For example, the CUS sites of RuO₂ are more active for OER than bridge sites,⁸ but the rate-determining step for the (100) and (11) facets are the removal of -OO from the CUS sites while for the (101) facets, OER rates are limited by the conversion of O to OOH species.⁶ On the other hand, for most facets of IrO₂,

the OER rate is limited by -O to -OOH conversion.⁷ Similarly, the understanding of (Fe,Co,Ni)-based oxides in alkaline conditions has advanced significantly,^{9–12} leading to the development of material descriptors such as the e_g band occupancy² and oxygen 2p-band center¹³ to guide the rational design of OER catalysts.¹ For example, Grimaud et al. have reported the synthesis of Pr_{0.5}Ba_{0.5}CoO₃, which has nearly the optimal oxygen 2p-band center to maximize the OER activity while remaining stable.¹⁴ Colin et al.¹⁵ have further shown that the oxygen 2p-band center of surface oxygens universally scales with the reactivity of the surface, regardless of whether the material is a face-centered cubic metal, rutile-structured oxide, or perovskite-structured oxide, corroborating some previous work by Xu and Kitchin that has suggested such a relationship.¹⁶ Furthermore, Kuznetsov et al. have shown that the addition of highly acidic cations such as Bi³⁺ increases the OER activity and stability of SrCoO_{3-x} due to the

Received: January 28, 2025

Revised: April 23, 2025

Accepted: April 24, 2025

inductive effect.¹⁷ Similar concepts have also been applied to Co¹⁸ and Ni-based^{10,19–21} layered double hydroxides, where incorporation of Fe³⁺ ions can increase the OER activity by two orders of magnitude. The current hypothesis for the significantly increased activity is that Fe is the active site in these materials, and the local electronic coupling of a surface Fe site with the metal hydroxide host²² and/or adjacent surface Fe sites¹¹ leads to significantly higher OER activity. Building even further, Yuan et al.²³ have reported Ni-based metal hydroxide organic frameworks (MHOFs) with three times the tunability of their pure hydroxide analogues. While the surface of these MHOFs transforms to oxyhydroxides under OER conditions,²⁴ their wide tunability still holds promise as a generalizable platform for further optimizing the electronic structure of OER catalysts. Unfortunately, despite the significant efforts to understand and optimize OER catalysts, the most active heterogeneous catalysts for OER are still at least an order of magnitude less active on a per active site basis than the oxygen-evolving complex found in photosystem II,³ highlighting opportunities for further catalytic activity enhancement. Recent work by Scott et al.²⁵ have shown that OER can occur on Ru and RuO_x as low as 1.3 V vs. the reversible hydrogen electrode (V_{RHE}) and with a Tafel slope of only 25 mV dec⁻¹, both of which can be readily captured through microkinetic modeling when the potential dependence of reaction intermediate coverage is considered.²⁵ As such, further experiments and computations will be necessary to unlock new chemistries that show high OER activities at 1.3 V_{RHE} or lower.

As a wide material space remains unexplored for catalysis, large data sets, such as the Open Catalysis Project^{26,27} and machine learning methods for predicting material properties,^{28,29} have been developed for aiding the virtual screening of such a space. For example, Ulissi et al. have developed a machine learning model for predicting surface Pourbaix diagrams, which are critical for understanding surface adsorbates and coverages at potentials of interest.³⁰ Ulissi et al. have also used machine learning to explore the active site and reactivity of different Ni–Ga alloy facets for CO₂ reduction, explaining previously published experimental results showing the reduction of CO₂ to value-added products like CH₄, C₂H₄, and C₂H₆ at low overpotentials on Ni_xGa.³¹ Furthermore, Calusen et al. have reported the use of machine learning for discovering highly active ORR high entropy alloys catalysts in the Ag–Ir–Pd–Pt–Ru composition space, predicting AgPd alloys to have about 3× higher activity than that of Pt.³² Recently, Lunger et al. have utilized machine learning to report per site level understanding of transition metal oxides for the OER and identified promising new candidates for highly active OER catalysts.³³ They report using crystal graph convolution neural networks²⁸ to extend the previously established O 2p-band center scaling of surface oxygens to apply to specific oxygens within the crystal structure and were able to correlate per site electronic/phononic properties with each other and the binding energies of OER intermediates. Out of the properties discussed, the 2p-band center and Bader charge of adsorbed oxygen had the strongest influence on binding energies, but how these properties can be controlled for future design of highly active OER catalysts is not discussed.

New methods are needed for discovering oxides with unique oxygen sites that are highly active for the OER, which could be achieved through metal substitution to create ternary or more complex oxides (e.g., high entropy oxides). The multi-

component nature of these complex oxides necessitates the development of high-throughput experimental methods that can evaluate their catalytic activity with high fidelity and at scale, which to this day have been significantly overshadowed in number by virtual screening methods. Reddington et al.³⁴ were the first to report a high-throughput experimental method for screening electrocatalysts, which used a pH-sensitive quinone dye within the electrolyte that would fluoresce based on the methanol oxidation activity of a compositional array. Since then, other fluorescence-based setups have also been developed for OER,^{35,36} oxygen reduction,³⁷ and methanol oxidation reactions.^{38,39} In addition to optical methods, other high-throughput screening methods include scanning flow/droplet cells^{40,41} that can sequentially test electrocatalysts that have been deposited on a conductive substrate, as well as a cell from Nuvant Systems that is able to test multiple electrodes simultaneously in separate potentiostat channels.⁴² However, previous reports of these high-throughput setups have used discrete compositions within a given chemical space, which can limit the insight gained as a majority of the activity–composition relationships will require interpolation, potentially omitting many compositions that may break typical scaling relations. We therefore aimed to develop a high-throughput OER catalyst screening setup that can measure the activity of an entire composition space simultaneously, which we believe could be achieved by using oxygen-sensitive fluorescence as a method for quantifying the amount of oxygen generated on a working electrode with composition gradients. Development of such a system would greatly accelerate the speed at which entirely unexplored continuous composition spaces can be screened for OER activity.

In this work, we detail a custom-built high-throughput setup for screening entire composition spaces of OER electrocatalysts using fluorescence to measure the amount of generated oxygen and epitaxial composition gradient films to represent entire composition spaces. Using the setup, the OER activity of the continuous composition space La_{0.6}Sr_{0.4}Fe_xCo_{1-x}O₃ (001) $x \in [0, 0.88]$ grown using combinatorial pulsed-laser deposition (PLD) was screened, which was chosen based on previous work showing that the end compositions fall on the opposing sides of the OER activity volcano with different rate-limiting steps (RLS).² For example, the typical RLS of OER on Co-active perovskites is the formation of peroxide ions from the deprotonation of oxyhydroxide groups ($\text{Co}^{(m)+}\text{-OOH}^- + \text{OH}^- \rightarrow \text{Co}^{(m+1)+}\text{-O}_2^{2-} + \text{H}_2\text{O} + \text{e}^-$), while the typical RLS of OER on Fe-active perovskites is the formation of oxyhydroxide species ($\text{Fe}^{(m+1)+}\text{-O}^{2-} + \text{OH}^- \rightarrow \text{Fe}^{(m)+}\text{-OOH}^- + \text{e}^-$).² We would therefore intuitively expect some intermediate composition to show OER activity higher than that of either end composition. As combinatorial PLD gave fine control of the composition as a function of space while ensuring the epitaxial growth of a homogeneous film,^{43,44} these composition gradient films could create surface oxygen sites not available for oxides with discrete oxide compositions^{33,45} and allow for a direct correlation of OER activity with composition changes. The setup was measured to have a minimum O₂ detection limit of ~2 nmol and was able to discern differences in the OER activity across the film composition gradient. The fluorescence intensities over single composition films were quantitative to the amount of O₂ generated and were used to transform the fluorescence intensities observed over the film to apparent OER rates.

Taken together, the results reported here show that the setup can accurately capture the differences in the OER activity across a continuous composition gradient, allowing for the screening of an entire composition space within a single measurement. Within the space tested, we found that oxide compositions near $\text{La}_{0.6}\text{Sr}_{0.4}\text{Fe}_{(x=0.2)}\text{Co}_{(1-x=0.8)}\text{O}_3$ are among the most active, as the compositions ranging from $x = 0.15$ – 0.25 showed comparable OER activity with a continuous change in activity measured across the entire range. The approximate optimal composition range for the OER within the tested $\text{La}_{0.6}\text{Sr}_{0.4}\text{Fe}_x\text{Co}_{1-x}\text{O}_3$ space was confirmed with density functional theory (DFT) calculations, which showed that increasing Co substitution on the $\text{La}_{0.5}\text{Sr}_{0.5}\text{Fe}_x\text{Co}_{1-x}\text{O}_3$ B-site terminated (001) surface decreases the required overpotential for the OER computed on both Fe and Co sites. At around and below $x = 0.35$, Fe becomes more active for OER than Co sites, highlighting that when designing new OER catalysts in the future, it is important to consider that the active site for OER can change with substitution, even when the active species is a minority in the structure.

EXPERIMENTAL DESIGN AND METHODS

In situ Fluorescence Imaging System. The *in situ* fluorescence imaging system (Figure 1a) was constructed within a black hardboard optical enclosure that provides two purposes. First, the enclosure is a safety measure against intense UV or near-UV illumination during experimentation, in addition to appropriate protective safety goggles. Second, the enclosure (along with the optical board) serves as a mechanical framework in which different components of the setup are mechanically secured. Fixing the optical components and spectroelectrochemical cell through the enclosure and the optical table simplifies recreating imaging conditions for consistent measurements. Illumination for fluorescence came from a 405 nm light-emitting diode (LED) mounted on standard optical posts (Thorlabs), where the LED output power was controlled to 1.7 W of continuous illumination during measurements. Wavelength and power of the LED were chosen to match the excitation characteristics of the commercial O_2 detection binary fluorescent paint (ISSP). Fluorescence images were collected using a CMOS color camera (Thorlabs) fitted with a machine vision zoom lens (Thorlabs), which was mechanically secured in place on the optical enclosure created using a black hardboard. A fixed focal length of 20 mm with an aperture of $f/4$ was used for all measurements, where the camera focus was manually controlled and fixed on the fluorescent dye-painted stainless steel mesh. A 495 nm long pass filter (Thorlabs) placed before the zoom lens was used to block the LED illumination for better contrast of the fluorescence signal. Standard half-inch optical posts and postholders were used to secure the LED in a fixed position relative to the spectroelectrochemical cell.

Spectroelectrochemical Cell. A home-built spectroelectrochemical cell (Figure 1b) was constructed by assembling top and bottom PTFE plates for the outer shell, a PTFE cover, stainless steel plates for mechanical stability, and fluorosilicone gaskets that serve as both a sealant and spacer. Components were assembled in a sandwich-like configuration (Figure 1c) in the order of bottom stainless steel plate, PTFE plate, fluorosilicone gasket #1, working electrode, fluorosilicone gasket #2, stainless steel mesh containing a binary fluorescence dye (hereafter referred to as the fluorescent detector, detailed preparation procedure can be found in SI), Ni mesh counter

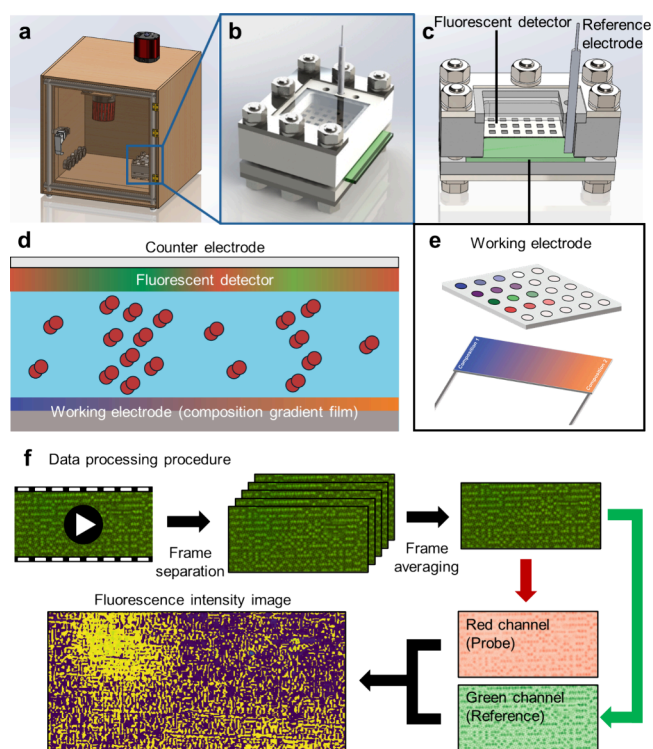


Figure 1. CAD representations of the setup and video processing method presented in the manuscript. (a) CAD design of the fluorescence imaging spectroelectrochemical setup with the CMOS camera, LED, and spectroelectrochemical cell secured in position. (b) CAD design of the spectroelectrochemical cell showing the square window at the top and holes for holding electrodes and gas tubes. (c) Cross section of the spectroelectrochemical cell showing the configuration of key components within the cell. (d) Schematic diagram demonstrating how the fluorescence OER setup is able to detect oxygen evolution using fluorescence. (e) Examples of working electrodes that the cell can accommodate. The top example consists of an array of catalysts deposited on an FTO substrate, while the bottom example consists of a composition gradient thin film electrode. (f) Outline of the workflow to process the videos that are collected during the OER to convert them from RGB space to fluorescence intensity following eq 1.

electrode (Precision Eforming, 30×30 mesh, Product number: MN8), PTFE top and cover, and a top stainless steel plate (Figure S1 shows an exploded diagram of the cell design). The Ni mesh counter electrode is rated to have a 90% transparency, minimizing interference with the detection of the fluorescence signal with the CMOS camera. The counter electrode is parallel to the working electrode to ensure a uniform Ohmic drop between the entire working electrode and the counter electrode. Nuts and bolts were used to ensure alignment and secure the components. The PTFE top and cover contain square windows for *in situ* imaging of the working electrode placed parallel to the window within the cell. Three holes in the PTFE cover were sized to match Ag/AgCl mini-reference electrodes (Pine Research).

The binary fluorescence paint contains a green reference color and a red probe color that can be used to track the O_2 generated from the OER. Under 405 nm illumination in the absence of O_2 , both the green reference and red probe fluoresce in their nominal color. The presence of O_2 selectively quenches only the fluorescence intensity of the red probe, making the fluorescence appear greener. The difference

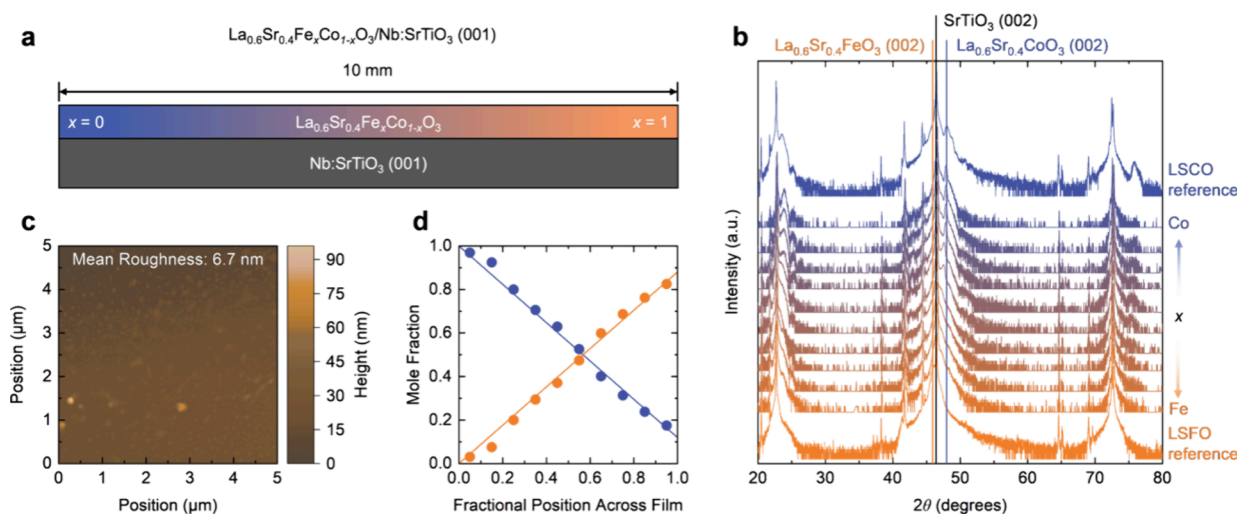


Figure 2. (a) Schematic diagram showing the arrangement of the $\text{La}_{0.6}\text{Sr}_{0.4}\text{Fe}_x\text{Co}_{1-x}\text{O}_3$ (001) composition gradient film grown on a Nb-doped SrTiO_3 (001) substrate. (b) XRD patterns taken at equal intervals across the film with increasing Co-content on higher spectra. Reference spectra of $\text{La}_{0.6}\text{Sr}_{0.4}\text{CoO}_3$ (LSCO) and $\text{La}_{0.6}\text{Sr}_{0.4}\text{FeO}_3$ (LSFO) grown on SrTiO_3 (001) are included at the top and bottom, respectively. (c) AFM image of the $\text{La}_{0.6}\text{Sr}_{0.4}\text{Fe}_x\text{Co}_{1-x}\text{O}_3/\text{Nb:STO}$ (001) composition gradient film. (d) WDS at equal intervals across the film showing the nearly linear composition change as a function of position.

between the green and red signals was then used as an indirect measure of the O_2 generation. The fluorescent detector was placed ~ 1 mm above and parallel to the working electrode. Using the color change of the fluorescent paint in the presence of O_2 , we could extract the O_2 generated from the working electrode could be extracted. As the intensity of the red probe signal can be increasingly quenched at higher concentrations of O_2 , the regions of the fluorescent detector that sit above regions of the electrode that are more active for the OER will therefore appear greener than regions of the fluorescent detector that sit above regions of the electrode that are less active for the OER, as illustrated in Figure 1d. The ability of the fluorescent detector to indirectly measure the OER activity from the local O_2 concentration above the working electrode enables the high-throughput nature of the setup. This cell design can accommodate and examine the OER activity of a working electrode (Figure 1e) consisting of discrete compositions deposited in an array-like fashion or with continuous composition gradients. Tests using a 3×3 array of $\text{Co}_4\text{Fe}_4\text{Ni}_2\text{O}_x$ of varying sizes deposited on a fluorine-doped SnO_2 electrode showed that the fluorescence intensities are localized above the OER active regions and are not significantly affected by the lateral diffusion of O_2 bubbles under the conditions that they are tested (details can be found in Supplementary Note 1).

Data Collection and Fluorescence Processing Procedure.

Electrochemical and fluorescence intensity data were both collected simultaneously in the electrochemical fluorescence setup and used to gather the OER activity as a function of film dimension or composition. The cell was positioned such that the fluorescent detector above the entire working electrode was captured simultaneously and homogeneously illuminated by the 405 nm LED. Prior to each test, the electrolyte was sparged with argon (Ar) for at least 20 min to remove any dissolved O_2 . In addition, the cell was placed into a nearly sealed, transparent high-density polyethylene bag, constantly refreshed with Ar for at least 20 min before and during the measurement. These two steps ensured that any fluorescence observed was attributed to the O_2 generated from

the working electrode and not from dissolved O_2 in the electrolyte and background O_2 from the atmosphere. Figure S2 shows the fluorescence evolution as a function of time from the fluorescent detector in the absence of the OER, confirming that there was minimal detection of the O_2 from the background or other sources. The working electrode was held at constant potentials between 1.2 and 1.8 V_{RHE} , where the electrochemical current and a continuous video (at 10 frames per second) of the fluorescence response were collected. As the thin film sample was electrically contacted by the same conductive substrate, the entire composition gradient was subjected to the same applied potential, allowing for the comparison of the OER activity of the entire composition space simultaneously. The videos were started 5 s before the electrochemical testing to collect background frames of the fluorescence. The videos were converted from raw video into fluorescence intensities following the procedure outlined in Figure 1f. First, the videos were separated into individual frames, and a single frame corresponding to the arithmetic average of the frames within a 1 s window of video was calculated to reduce noise (i.e., every 10 frames starting from frame 50 were averaged). To convert the RGB color space images to meaningful fluorescence images and intensities, the intensities of the red and green signals of each averaged image were extracted, while the intensity of the blue signal was effectively discarded. Figure S3 shows representative images of the extracted red, green, and blue signals. As expected, based on the supposed emission of the fluorescent dye, intensities of the red and green signals were observed, while the intensities of the blue signal were low. The fluorescence intensity of each pixel was then calculated following equation [1],

$$\text{fluorescence} = -(\text{green} - \text{red})_{t'} + (\text{green} - \text{red})_{t_0} \quad (1)$$

where *fluorescence* refers to the fluorescence intensity, and *green* and *red* refer to the intensity of the green reference and red probe signals, respectively, of averaged images taken at the time t indicated by the subscripts. t_0 refers to the time of the background image acquisition, while t' refers to the image

capture time such that $t' > t_0$. The negative and positive signs preceding the t' and t_0 terms are so that the resulting fluorescence positively correlates with increased O₂ detection.

Continuous Composition Gradient Film Synthesis. Combinatorial pulsed-laser deposition was used to deposit the La_{0.6}Sr_{0.4}Fe_xCo_{1-x}O₃ composition gradient films on 5 × 10 mm 0.5 wt % Nb-doped SrTiO₃ (Nb:STO) (001) and (111) substrates, where the composition gradient is parallel to the 10 mm dimension. The deposition conditions were controlled to ensure epitaxial growth on the substrates and maximize the homogeneity and flatness of the film so that any observed changes in the OER activity across the film could be primarily ascribed to changes in the intrinsic OER activity of different compositions.⁴⁶ For perovskite-structured oxides, the (001) facet tends to be more stable than the (111) facet;⁴⁷ as such, the (001) films were the main focus of this work. However, the Supporting Information contains data on tests with (111) faceted films.

RESULTS AND DISCUSSION

Characterization of Composition Gradient Working Electrodes. The successful epitaxial deposition of the La_{0.6}Sr_{0.4}Fe_xCo_{1-x}O₃ composition gradient on the Nb:STO substrate (001) ($a = 3.905 \text{ \AA}$) (Figure 2a) was confirmed by X-ray diffraction (XRD). Since a monochromator was not used for these measurements, the SrTiO₃ (001), (002), and (003) reflections due to K_α radiation were observed around $2\theta = 23$, 46, and 73°, respectively, with each accompanied by reflections due to K_β radiation at slightly lower 2θ values (around 20°, 42°, and 65°, respectively). Adjacent to the K_α peaks, peaks corresponding to the La_{0.6}Sr_{0.4}Fe_xCo_{1-x}O₃ can be observed to the right or left, depending on whether the composition is Co-rich or Fe-rich, respectively. For example, a peak around 48° grew in intensity with more Co substitution, matching well with the (002) reflection of La_{0.6}Sr_{0.4}CoO₃, as indicated by the La_{0.6}Sr_{0.4}CoO₃ reference spectrum (Figure 2b, top spectrum). Conversely, the intensity of the peak around 46° also increased with higher Fe substitution, in agreement with the La_{0.6}Sr_{0.4}FeO₃ reference spectrum (Figure 2b, bottom spectrum). Homogeneous and flat film surfaces were revealed by atomic force microscopy (AFM) (Figure 2c), where the average roughness was measured to be 6.7 nm. Moreover, wavelength dispersive X-ray spectroscopy revealed that the mole fraction of Co:Fe decreased linearly across the film length, where the midpoint showed a near 1:1 ratio of Co:Fe (Figure 2d). Constrained linear fits of the compositions as a function of the position across the film such that at $x = 0$, the Co fraction was unity were used to estimate the composition of the film. A constrained fit was used since using the best fit linear line would result in unphysical compositions (i.e., negative Fe substitution, such as La_{0.6}Sr_{0.4}Fe_{-0.375}Co_{1.0375}O₃) near the end of the films (as shown in Figure S4). The relative Co (x_{Co}) and Fe (x_{Fe}) mole fractions as a function of distance across the film d were fit to be

$$x_{\text{Co}} = 1 - (0.88 \pm 0.05)d$$

$$x_{\text{Fe}} = (0.88 \pm 0.05)d$$

where the uncertainties were extracted from the 95% confidence bounds of the fits (Figure S9). Based on the characterization, a homogeneous, epitaxial film with a nearly linear composition gradient similar to a single-crystal material was successfully grown. We can therefore attribute any

observed differences in the OER activity almost entirely to changes in the composition as the reaction was confined to just the surface. Similar depositions were also carried for (111) orientation films; the characterization of these films can be found in Figure S5.

Spectroelectrochemical Measurements of La_{0.6}Sr_{0.4}Fe_xCo_{1-x}O₃/Nb:SrTiO₃ (001). The La_{0.6}Sr_{0.4}Fe_xCo_{1-x}O₃/Nb:SrTiO₃ (001) films were measured in the spectroelectrochemical cell to probe how the OER activity changed with the composition. Cyclic voltammetry (CV) was first conducted, which showed an onset potential for OER around 1.55 V_{RHE} (Figure S6), which is in agreement with Co and/or Fe-based perovskites as reported previously.^{2,13,17} When held at constant potentials, the oxidation current densities measured at 1.2, 1.3, and 1.4 V_{RHE} were found to decay sharply with time and reach similar steady-state values. In contrast, increasing the applied voltage to 1.5 V_{RHE} or higher led to much greater current densities than those at lower voltages, indicating the onset of the OER. The OER oxidation current density of the film (Figure 3b) at 1.5 V_{RHE} and above was found to increase exponentially with increasing applied voltage, with a Tafel slope of ~140 mV dec⁻¹.

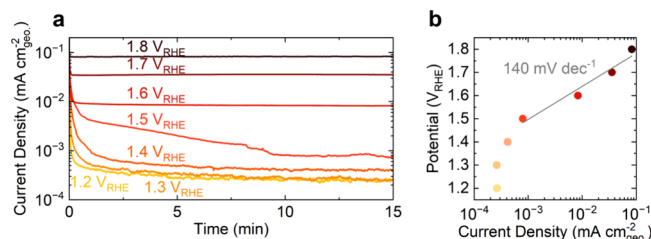


Figure 3. Electrochemistry of the La_{0.6}Sr_{0.4}Fe_xCo_{1-x}O₃/Nb:STO (001) films. (a) Chronoamperometry of the films from 1.2 to 1.8 V_{RHE} for 15 min at each potential. (b) Tafel plot of the OER activity of the films using the current measured after 10 min at each potential. A linear line was fit for the data points measured at 1.5 V_{RHE} or higher to estimate the Tafel slope of the film.

The fluorescence measurements of the La_{0.6}Sr_{0.4}Fe_xCo_{1-x}O₃/Nb:STO (001) film revealed a clear composition-dependent OER activity. Figure 4 shows the fluorescence intensity evolution (with a viridis color map applied) of the film after 1, 5, and 10 min at selected potentials. No clear fluorescence was observed from 1.1 through 1.6 V_{RHE}, while the onset of OER current densities in the electrochemical measurements commenced at 1.5 V_{RHE}. At applied potentials of 1.7 V_{RHE} or higher, a clear fluorescence increase above the background was observed on the Co-rich side of the La_{0.6}Sr_{0.4}Fe_xCo_{1-x}O₃ space. When the potential was further raised to 1.8 V_{RHE}, the same fluorescence remains concentrated on the Co-rich side of the film (bottom row in Figure 4), agreeing with the fluorescence results observed at 1.7 V_{RHE} and suggesting that the OER activity is higher for Co-rich compositions in the La_{0.6}Sr_{0.4}Fe_xCo_{1-x}O₃ composition space. Furthermore, as can be seen by the 5 min column in Figure 4 (middle column), the fluorescence appears to be more intense at 1.8 V_{RHE} than at 1.7 V_{RHE}, which is consistent with the higher current measured at the higher potential.

We postulate that the O₂ detected by the fluorescent detector is not dissolved in the electrolyte but rather O₂ bubbles, which is supported by the following arguments. First, at 1.6 V_{RHE}, no fluorescence intensity above the background

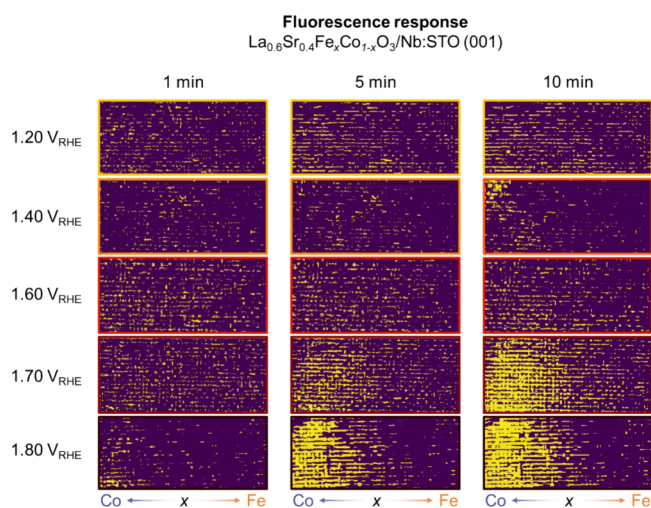


Figure 4. Fluorescence intensities detected over $\text{La}_{0.6}\text{Sr}_{0.4}\text{Fe}_x\text{Co}_{1-x}\text{O}_3/\text{Nb:STO}$ (001) at 1, 5, and 10 min at different applied potentials, where the left edge corresponds to $\text{La}_{0.6}\text{Sr}_{0.4}\text{CoO}_3$ and the right edge is $\text{La}_{0.6}\text{Sr}_{0.4}\text{FeO}_3$. A viridis color map was applied to each image.

was observed, yet the amount of O_2 based on the total charge passed surpassed the solubility limit of the electrolyte volume about 80 s after the potential was applied (Figure S7a).

Furthermore, at 1.7 V_{RHE} , increased fluorescence above the background became pronounced when the amount of generated oxygen, based on the measured charge, was about an order of magnitude higher than the solubility limit of O_2 in the electrolyte volume between the working electrode and fluorescent detector (Figure S7b), assuming 100% Faradaic efficiency toward OER). That is, fluorescence of generated O_2 came after the potential was applied for 4 min, which is about 6x the time needed to saturate the electrolyte volume between the working electrode and fluorescent detector (Figure S7b), assuming full dissolution of generated O_2 . These estimations assume a uniform production of oxygen over the composition gradient. However, the observed fluorescence strongly suggests a higher local concentration of O_2 above the Co-rich side, which would saturate the local electrolyte volume on the Co-rich side even faster than our estimations assuming uniform generation of O_2 , further strengthening our hypothesis. Therefore, the fluorescent detector can detect O_2 bubbles generated at high overpotentials, but it appears not to be sensitive to dissolved O_2 in the electrolytes generated at low potentials. Details about these calculations can be found in the Supporting Information.

Fluorescence intensity mapping across the films provides direct insight into the composition dependence of the OER activity in the $\text{La}_{0.6}\text{Sr}_{0.4}\text{Fe}_x\text{Co}_{1-x}\text{O}_3$ (001) composition space. Therefore, the intensity of each column of pixels was averaged as a function of the applied potential and time to generate a

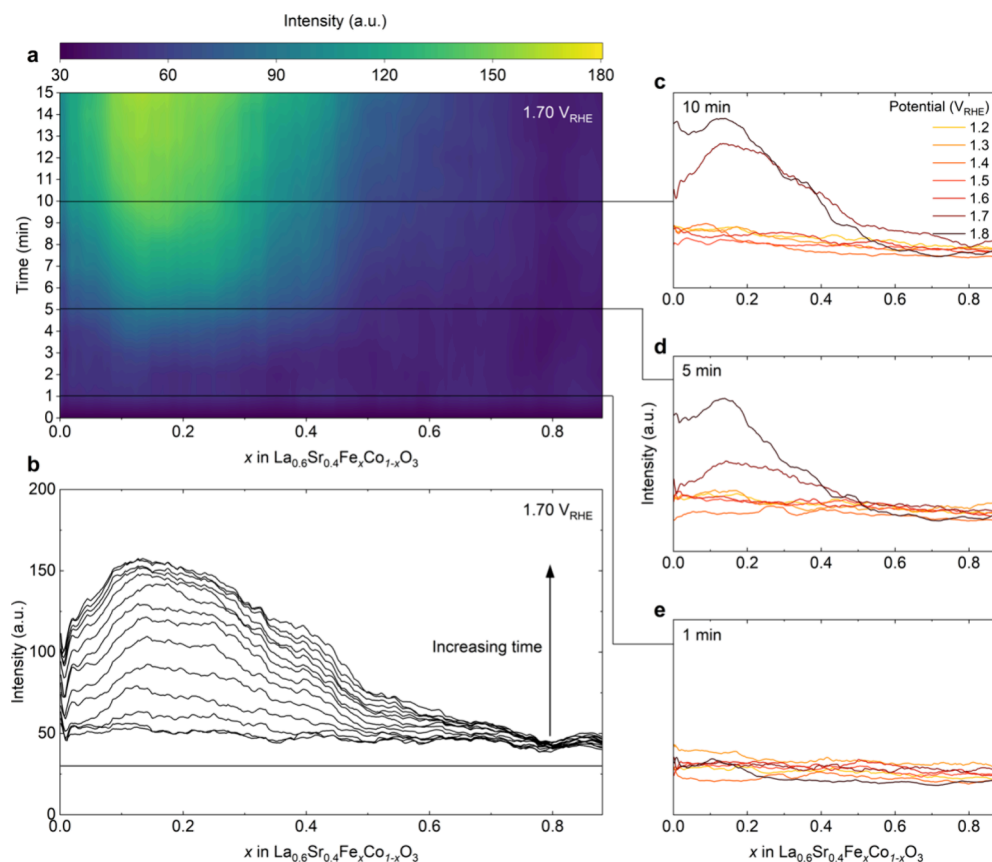


Figure 5. Fluorescence intensity of $\text{La}_{0.6}\text{Sr}_{0.4}\text{Fe}_x\text{Co}_{1-x}\text{O}_3/\text{Nb:STO}$ (001) as a function of time and applied potential. (a) Heat map showing the fluorescence evolution across the film when held at 1.70 V_{RHE} for 15 min. (b) Flattened visualization showing the evolution of the peak position at approximate $x = 0.15$ as a function of time. (c) Fluorescence spectra taken after being held at various potentials from 1.2 to 1.8 V_{RHE} for 10 min. (d) Fluorescence spectra taken after being held at various potentials from 1.2 to 1.8 V_{RHE} for 5 min. (e) (Lack of) fluorescence taken after being held at potentials from 1.2 to 1.8 V_{RHE} for 1 min.

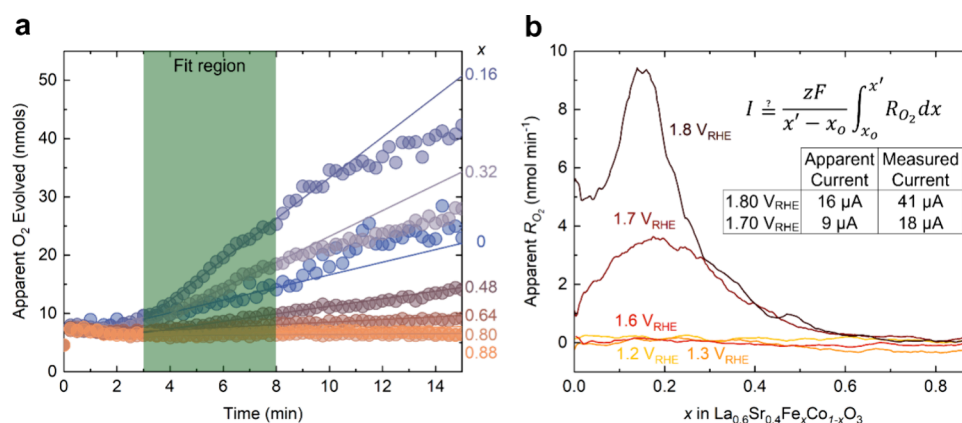


Figure 6. Apparent O₂ evolution rates from the fluorescence intensity data. (a) Extracted amounts of apparent O₂ generated at 1.7 V_{RHE} as a function of time for representative compositions within the La_{0.6}Sr_{0.4}Fe_xCo_{1-x}O₃ (001) gradient with linear fits from 3 to 8 min (shaded region). The apparent O₂ generated was extracted by converting the fluorescence intensity to O₂ generated using the fluorescence intensity as a function of O₂ generated for the single composition of La_{0.6}Sr_{0.4}CoO₃ film. (b) Apparent O₂ evolution rate R_{O₂} at various potentials as a function of *x* in La_{0.6}Sr_{0.4}Fe_xCo_{1-x}O₃. The inset table shows the apparent total current obtained from integrating R_{O₂} according to the equation compared to the directly measured current from the potentiostat.

single intensity corresponding to that composition slice. As the width of the film is about 700 pixels, each column of pixels corresponds to an approximate composition increment of $\Delta x = 1.3 \times 10^{-3}$. Figure 5a shows a representative contour map of fluorescence intensities measured across the film as a function of time when 1.7 V_{RHE} was applied. Aligning with the raw fluorescence images at 1.7 V_{RHE}, fluorescence intensity around $x = 0.15$ emerges after 4 min, which continued to grow with longer times. Lower potentials displayed negligible changes in fluorescence intensity as a function of time (Figure S8). Flattening the contour map (Figure 5b) confirms that a peak centered near $x = 0.15$ emerged after about 4 min, continued to grow for the subsequent 6 min, and reached steady state (e.g., reaching 150 fluorescence intensity units at $x = 0.15$) for the remaining 5 min. Figure S9 shows the fluorescence intensity collected on the film at the end of each chronoamperometry measurement (15 min). In contrast, the fluorescence intensities in the composition range from $x = 0.40$ to 0.70 continued to increase throughout the entire 15 min. A negligible change in the fluorescence intensity was observed for compositions with $x \geq 0.70$, suggesting that the OER activity of these compositions was not high enough to trigger a fluorescence response.

When the potential was further increased to 1.8 V_{RHE}, fluorescence grew faster and to higher intensities, while the composition-dependent fluorescence contour was in agreement with that observed at 1.7 V_{RHE}. For example, fluorescence was observed after 1 min at 1.8 V_{RHE} in contrast to 4 min at 1.7 V_{RHE} (Figure S10), with a peak centered around $x = 0.11$. The peak of fluorescence originally centered at $x = 0.11$ was found to shift to $x = 0.15$ after 4 min, which remained for the rest of the experiment and agrees with the peak location observed at 1.7 V_{RHE}. In addition, the maximum intensity observed at 1.8 V_{RHE} across the entire 15 min is about 20 fluorescence intensity units higher than that at 1.7 V_{RHE} (Figure S10), in agreement with the higher OER current observed at the higher potential. The same experiments were carried out by using (111) oriented films of the same composition space. The (111) film showed higher OER currents compared to the (001) film at the same applied potential, indicating higher OER activity of the (111) facet (Figure S11). A peak centered

around $x = 0.22$ was observed for the (111) oriented film at both 1.7 and 1.8 V_{RHE} (Figure S12a,b, respectively), which is about 5% higher Fe substitution compared to the (001) film. Interestingly, a smaller peak around $x = 0.75$ was observed, potentially suggesting a secondary region of moderate OER activity for the (111) facet. If confirmed to be true, the secondary peak around $x = 0.75$ would suggest a region that does not conform to typical scaling relations, further demonstrating the utility of the setup in identifying unknown regions of interest worth studying.

Extracting Apparent OER Rates. The fluorescence intensity of the composition gradient film as a function of potential and time was converted to the amount of O₂ evolved using the fluorescence kinetics data collected on La_{0.6}Sr_{0.4}CoO₃ single composition films (see Figure S13). For potentials below 1.7 V_{RHE}, an absence of O₂ evolution was observed, as expected based on the fluorescence data collected at these potentials. At 1.7 V_{RHE}, the amount of apparent O₂ evolution increased for certain compositions but remained relatively constant for other compositions within the composition space (Figure 6a). A linear line was fit near the onset of the O₂ detection for each composition and applied potential to estimate the apparent OER rate (R_{O₂}), which are summarized in Figure 6b for 1.2, 1.6, 1.7, and 1.8 V_{RHE}. At both 1.7 and 1.8 V_{RHE}, a peak centered around $x = 0.15$ –0.20 was observed, where the extracted R_{O₂} for 1.8 V_{RHE} are generally larger than the extracted R_{O₂} for 1.7 V_{RHE}, consistent with 1.8 V_{RHE} also displaying higher OER currents than 1.7 V_{RHE} in the electrochemical data.

The extracted R_{O₂} values were integrated as a function of substitution and converted to currents (assuming 100% Faradaic efficiency toward 4e⁻ transfer OER) as a function of the *x*-substitution level to check for reasonable agreement between the calculated apparent currents and measured currents at 10 min (Figure 6b, inset). In general, the calculated currents are about half the measured currents, with the calculated currents being 9 and 16 μA at 1.7 and 1.8 V_{RHE}, respectively, while the measured currents are 18 and 41 μA at 1.7 and 1.8 V_{RHE}, respectively. Lower calculated currents compared to measured currents are physically realistic,

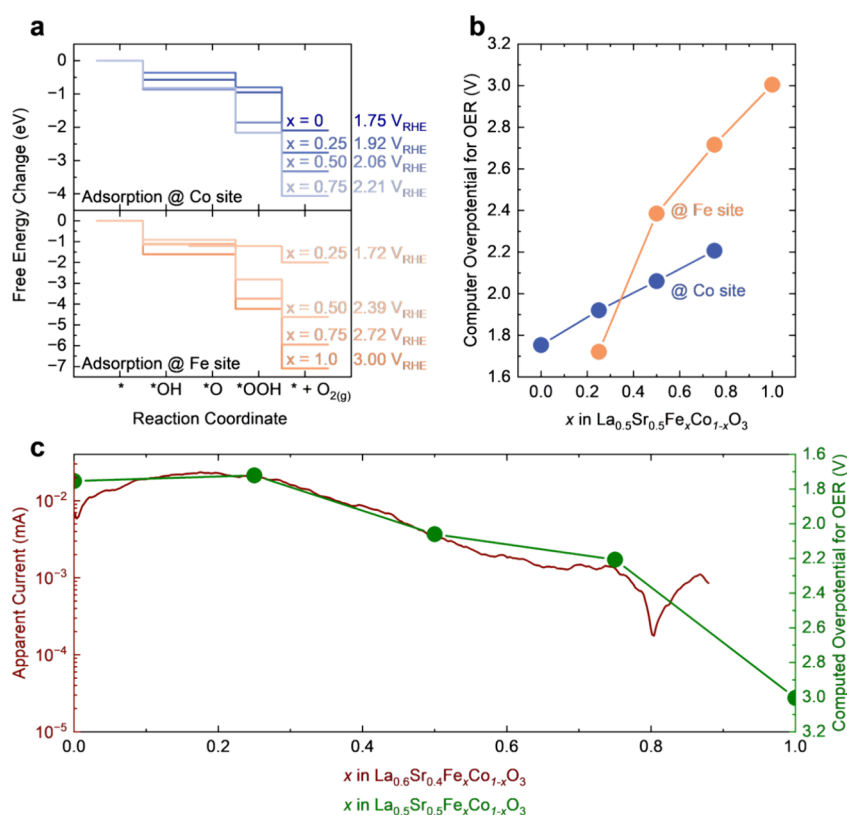


Figure 7. Energetics of the OER on selected compositions within the $\text{La}_{0.5}\text{Sr}_{0.5}\text{Fe}_x\text{Co}_{1-x}\text{O}_3$ (001) chemical space. (a) Reaction energetics for the OER plotted at the lowest potential required for the reaction to be downhill on the Co sites (top) and Fe sites (bottom). (b) Computed overpotentials of OER as a function of Co:Fe ratio on the Co and Fe sites. (c) Lowest computed overpotential for OER on the $\text{La}_{0.5}\text{Sr}_{0.5}\text{Fe}_x\text{Co}_{1-x}\text{O}_3$ (001) surface overlaid with the apparent OER current extracted from the fluorescence measurements.

suggesting that the setup is measuring the O_2 generated from the film, and not measuring other sources of O_2 , nor O_2 that does not exist. Our current setup therefore has an O_2 detection efficiency slightly below 50%. The fact that only about half of the generated O_2 is detected by the system also explains why no significant fluorescence intensity was detected at 1.5 and 1.6 V_{RHE} , despite the OER activity that can be measured electrochemically. Most likely, the rate of the OER at 1.5 and 1.6 V_{RHE} was too low for the generated O_2 to reach the critical concentration needed for the fluorescent detector to detect it. A collection efficiency of 50% is comparable to that of the rotating-ring disk electrode,^{48–50} a technique commonly used to detect the oxygen reduction and evolution reactions but without any spatial resolution. While other techniques with spatial resolution, such as scanning electrochemical microscopy, can boast high collection efficiencies, a $\sim 10 \mu\text{m}$ diameter probe needs to be within $60 \mu\text{m}$ of the electrode surface to reach a collection efficiency of $\sim 50\%$.⁵¹ Characterizing the activity of the working electrode with such a small tip will, therefore, take considerable time. Our fluorescence-based method enables fast, spatially resolved detection of O_2 with collection efficiencies comparable to space-blind techniques. Nonetheless, further improvements to the setup would include devising a fluorescent detector that is more sensitive to oxygen so that lower potentials can be applied, allowing for more information to be collected from a single experimental set.

Computation and Identifying the Most Active Composition within $\text{La}_{0.6}\text{Sr}_{0.4}\text{Fe}_x\text{Co}_{1-x}\text{O}_3$ (001). The observed composition dependence of the OER activity as a function of composition within the LSCFO (001) space was

validated using density functional theory (DFT) computation, which showed good qualitative agreement with the experiments. To simplify the computation, the A-site composition was set to be (La, Sr) = (0.5, 0.5), which may have an effect on the absolute values computed but should not change the overall trends observed. Substitution intervals of $x = 0.25$ from [0,1] were used, and the overpotential of OER was calculated from the reaction energetics (Figure 7a). The computation revealed that the material stability of the composition space is not strongly dependent on the B-site ordering (Figure S15). However, the OER activity is a strong function of the B-site ordering within the structure (Figures S16–S19), where the overpotential for the same substitution can differ by over 1 eV (summarized in Figure S20). For example, at $x = 0.25$ on the Fe site, if the Fe atoms are arranged diagonally from each other, then the overpotential was calculated to be ~ 3.2 eV, while the overpotential is only ~ 1.72 eV when the Fe atoms are columnar. All the binding energies of the calculated adsorbates follow scaling relations, indicating that the calculated energetics can accurately capture trends (Figure S21).

Looking at only the lowest calculated overpotential for all tested configurations, the Co-site becomes less active (i.e., higher overpotential) with increased Fe substitution, while the Fe sites increase in activity with less Fe substitution (Figure 7b). Interestingly, a crossover point around $x = 0.35$ was observed where the Fe sites become more active than the Co sites for OER, which aligns with previous studies suggesting that Fe is the active site in $\text{Co}_x\text{Fe}_{1-x}\text{O}_y\text{H}_z$ catalysts.¹⁸ Overlaying the lower calculated overpotential between the

Co and Fe sites as a function of composition displayed a qualitative trend similar to the apparent OER activity measured from the fluorescence measurements (Figure 7c). A slight decrease in the OER overpotential was observed going from $x = 0$ to $x = 0.25$ (from 1.75 to 1.72 V_{RHE} , respectively). However, further Fe substitution led to a monotonic decrease in the OER activity, with the pure Fe perovskite showing a large overpotential of 3.00 V_{RHE} , agreeing with the lack of fluorescence observed on the Fe-rich side of the film.

The measured apparent OER currents from the fluorescence measurements in conjunction with the computation therefore show that compositions near $\text{La}_{0.6}\text{Sr}_{0.4}\text{Fe}_{(x=0.2)}\text{Co}_{(1-x=0.8)}\text{O}_3$ ($x \pm 0.05$) (001) are among the most active within the $\text{La}_{0.6}\text{Sr}_{0.4}\text{Fe}_x\text{Co}_{1-x}\text{O}_3$ (001) chemical space. Previous results from Wang et al. studying the same chemical space, but as powders of discrete compositions⁵² also found that a maximum in OER activity occurs around $x = 0.20$ and that the Fe-rich side generally shows lower activity compared to the Co-rich side, in agreement our findings (compared in Figure S22). While the exposed facets of the particles were not characterized, since the (001) facet of similar perovskites tends to be the most energetically favorable,⁴⁷ the particles are representative enough to further validate the observed fluorescence trends. Of significance is the contrast with the work from Burke et al.¹⁸ that shows the maximum OER activity of $\text{Co}_{1-x}\text{Fe}_x\text{O}_y\text{H}_2$ catalysts around $x = 0.5$, rendering similar oxidation states for Co and Fe in $\text{La}_{0.6}\text{Sr}_{0.4}\text{Fe}_{(x=0.2)}\text{Co}_{(1-x=0.8)}\text{O}_3$ ($x \pm 0.05$). The qualitative trend agrees with our study, where the OER activity displays an initial increase with Fe substitution, followed by a decrease once a critical substitution level is reached.

Implication of High-Throughput Catalyst Screening Techniques. The change in the active site from Co to Fe with lower Fe substitution indicates that the reactivity of a composition cannot simply be thought of as a linear interpolation between similar compositions. As the activity of the Fe site in $\text{La}_{0.6}\text{Sr}_{0.4}\text{Fe}_{0.25}\text{Co}_{0.75}\text{O}_3$ was found to surpass the activity of Co in $\text{La}_{0.6}\text{Sr}_{0.4}\text{CoO}_3$ despite $\text{La}_{0.6}\text{Sr}_{0.4}\text{FeO}_3$ being inactive for the OER, our results show that the local chemical environment near an active site can profoundly influence the reactivity of the atoms. Previous studies have suggested that Fe sites in CoFe-based catalysts are responsible for the enhanced activity over pure Co catalysts.¹⁸ However, the compositional dependence of the identity of the active site and underlying mechanism for the high activity of Fe only when mixed with Co has not been elucidated. In addition, our results reaffirm the hypothesis that the same bulk compositions could potentially have drastically different OER activities due to local ordering of the atoms within the crystal structure, a relatively unexplored handle for tuning catalysis.³³ Understanding the relationship between local ordering and activity could unlock unprecedented methods for engineering highly active catalysts. As such, we believe that the development of high-throughput catalyst screening techniques is not only critical for identifying compositions with high activity but will also motivate future fundamental studies to uncover new insights governing catalysis and catalyst design. The development of high-throughput screening tools will be crucial to determine interesting compositions within the vast unexplored chemical space for these fundamental studies.

The setup detailed here therefore holds great promise as a potential avenue worth optimizing for the future screening of composition spaces. Combining high spatial and time

resolution with a continuous compositional gradient library can allow for greatly accelerated screening of entire composition spaces for reactions beyond OER by modifying the setup. For example, using the same pH-sensitive fluorescence dye as Reddington et al.³⁴ could allow for the screening of methanol oxidation catalysts. Similarly, methanol-sensitive organic fluorophores could be used to screen catalysts for the reduction of CO_2 to methanol. In addition to electrocatalysis, the setup we report could also be adapted for screening reactions initiated by other stimuli, such as photocatalysis, thermocatalysis, and enzymatic catalysis by changing the stimulus source and fluorescent probe. Second, other modules could also be included to collect information about the composition space beyond catalytic activity. For example, the cell could be coupled with automated Raman or infrared spectroscopy mapping to study the structural evolution of the catalyst while screening their activity. Having a large database of coupled structural-activity information would be invaluable for machine learning/artificial intelligence (ML/AI) models to discover (potentially high-dimensional) descriptors of catalysts that are difficult for humans to parse.

Improvements to the setup will be required to realize such future applications. For example, it is critical to decrease the detection limit. We were able to detect O_2 only 1.7 V_{RHE} or higher, well beyond the onset of the OER. Optimizing the equipment, such as developing more sensitive fluorescent probes or photodetectors, could help. Another potential avenue worth exploring is directly dissolving a fluorescent dye into the electrolyte solution, which would forego the need for the dissolved O_2 to detach from the working electrode surface and travel to the fluorescent detector. However, convection currents of the electrolyte due to bubbles or natural diffusion of the dye in the electrolyte could present other problems that will need to be carefully controlled. Also, the current setup was able to use fluorescence to collect only potentiostatic electrochemical information about the sample, as the fluorescence response was not fast enough. However, in some cases, transient information may be more useful for evaluating catalytic activity. Decreasing the detection limit would potentially help for transient measurements to be collected, further increasing the information that can be gathered from this setup.

CONCLUSIONS

We report the design and implementation of a simple spectroelectrochemical cell for the screening of the OER catalysts using *in situ* fluorescence detection. Combining the cell with combinatorial PLD, we were able to screen an entire continuous composition space simultaneously, forgoing the need to use linear interpolation to predict the activity of compositions that are not tested in a typical discrete composition array. Using $\text{La}_{0.6}\text{Sr}_{0.4}\text{Fe}_x\text{Co}_{1-x}\text{O}_3/\text{Nb:STO}$ (001) as a model system to demonstrate the capabilities of the setup, a clear compositional-dependent fluorescence evolution within the continuous space was observed. Coupling single composition $\text{La}_{0.6}\text{Sr}_{0.4}\text{CoO}_3/\text{Nb:STO}$ (001) films that acted as reference samples with the electrochemical measurements, the kinetics of the fluorescence signal were measured to quantitatively correlate the fluorescence intensity with the amount of O_2 evolved. In turn, this allowed us to transform the measured fluorescence intensities across the entire composition space into apparent O_2 evolution rates, where we found that the highest OER activity within the space is when 20% Fe

is substituted for Co. DFT calculations confirmed the trend observed from the fluorescence response. The computation also revealed that the overpotential for the OER within this space is highly dependent on the B-site ordering and that at $x = 0.25$, the Fe sites can actually be more active than Co sites for the OER. The change in the active site as a function of Fe substitution demonstrates that when screening new materials for the OER activity, simply linear interpolating of end compositions is not sufficient, demonstrating the need for further advancement of high-throughput screening methods. As more robust ML/AI models aimed at materials discovery are developed, it is crucial that high-throughput screening tools are ready not only for supplying data to train the models but also to validate model predictions. This study outlines the high resolution, accuracy, and ease of use of an *in situ* fluorescence-based setup for OER catalyst screening, laying the foundation for the development of a future high-throughput yet accurate, quantitative assessment method of catalyst discovery for OER and beyond.

■ ASSOCIATED CONTENT

SI Supporting Information

The Supporting Information is available free of charge at <https://pubs.acs.org/doi/10.1021/acscatal.5c00702>.

Supplementary experimental methods; fluorescence kinetic measurements and calculating first-order approximation for O₂ solubility limit in the electrolyte volume between the working electrode and fluorescent detector; DFT calculation; assessment of lateral spread of fluorescence; supplementary figures of exploded diagram of the custom cell, fluorescence evolution at open circuit potential, representative RGB images, fits of the Co:Fe ratio as a function of position on the film, cyclic voltammetry of the composition gradient film, time required to reach solubility limit of electrolyte, fluorescence responses from 1.1 to 1.8 V_{RHE}, fluorescence kinetics measured on single composition La_{0.6}Sr_{0.4}CoO₃ films, DFT computation, and fluorescence of a 3 × 3 array of Co₄Fe₄Ni₂O_x (PDF)

Fluorescence videos (ZIP)

Output files from the computation conducted in this study (ZIP)

■ AUTHOR INFORMATION

Corresponding Author

Yang Shao-Horn – Department of Materials Science and Engineering, Research Laboratory of Electronics, Department of Mechanical Engineering, and Department of Chemistry, Massachusetts Institute of Technology, Cambridge, Massachusetts 02139, United States; orcid.org/0000-0001-8714-2121; Email: shaohorn@mit.edu

Authors

Daniel J. Zheng – Department of Materials Science and Engineering, Massachusetts Institute of Technology, Cambridge, Massachusetts 02139, United States; orcid.org/0000-0002-9471-6856

Haldrian Iriawan – Department of Materials Science and Engineering, Massachusetts Institute of Technology, Cambridge, Massachusetts 02139, United States; orcid.org/0000-0002-2997-1180

Rohit Pant – Department of Materials Science and Engineering, University of Maryland, College Park, Maryland 20742, United States; orcid.org/0000-0002-4591-5752

C. John Eom – Research Laboratory of Electronics, Massachusetts Institute of Technology, Cambridge, Massachusetts 02139, United States; orcid.org/0000-0002-5481-294X

Hongbin Xu – Department of Materials Science and Engineering, Massachusetts Institute of Technology, Cambridge, Massachusetts 02139, United States; orcid.org/0009-0007-6311-475X

Jiayu Peng – Department of Materials Science and Engineering, Massachusetts Institute of Technology, Cambridge, Massachusetts 02139, United States; orcid.org/0000-0003-3696-770X

Cat Arase – Department of Mechanical Engineering, Massachusetts Institute of Technology, Cambridge, Massachusetts 02139, United States

Ichiro Takeuchi – Department of Materials Science and Engineering and Maryland Quantum Materials Center, Department of Physics, University of Maryland, College Park, Maryland 20742, United States; orcid.org/0000-0003-2625-0553

Yuriy Román-Leshkov – Department of Chemical Engineering and Department of Chemistry, Massachusetts Institute of Technology, Cambridge, Massachusetts 02139, United States; orcid.org/0000-0002-0025-4233

Complete contact information is available at: <https://pubs.acs.org/doi/10.1021/acscatal.5c00702>

Author Contributions

Y.S.-H., D.J.Z., and C.J.E. conceived the original study. D.J.Z. and C.J.E. designed and constructed the custom-built fluorescence cell with assistance from C.A. R.P. synthesized and characterized the composition gradient films with supervision from I.T.. D.J.Z. performed the fluorescence measurements of composition gradient and single composition films. D.J.Z. performed data analysis to extract fluorescence intensities with assistance from C.J.E. D.J.Z. transformed the fluorescence intensity into apparent OER reaction rates. H.I. performed the DFT computation with assistance from J.P., D.J.Z., and Y.S.-H. drafted the manuscript. All authors contributed to the revision of the manuscript.

Notes

The authors declare no competing financial interest.

■ ACKNOWLEDGMENTS

This work was supported by the Toyota Research Institute through the Accelerated Materials Design and Discovery Program, the Department of Energy, Advanced Research Projects Agency-Energy (ARPA-E) under Award Number DE-AR0001220, and Center for Electrochemical Dynamics and Reactions at Surfaces, an Energy Frontier Research Center funded by the U.S. Department of Energy, Office of Science, Basic Energy Sciences under Award # DE-SC0023415. The work at the University of Maryland was supported by NIST Cooperative Agreement 70NANB23H226. The authors would like to thank Dr. Shuo Wang (MIT) for assisting with the computation and Prof. Rafael Gomez-Bombarelli (MIT), Dr. Benjamin J. Blazsik (University of Chicago and Argonne National Lab), and Dr. Deborah J. Myers (Argonne National Lab) for helpful discussions.

REFERENCES

- (1) Hong, W. T.; Risch, M.; Stoerzinger, K. A.; Grimaud, A.; Suntvich, J.; Shao-Horn, Y. Toward the Rational Design of Non-Precious Transition Metal Oxides for Oxygen Electrocatalysis. *Energy Environ. Sci.* **2015**, *8* (5), 1404–1427.
- (2) Suntvich, J.; May, K. J.; Gasteiger, H. A.; Goodenough, J. B.; Shao-Horn, Y. A Perovskite Oxide Optimized for Oxygen Evolution Catalysis from Molecular Orbital Principles. *Science* **2011**, *334* (6061), 1383–1385.
- (3) Kuznetsov, D. A.; Han, B.; Yu, Y.; Rao, R. R.; Hwang, J.; Román-Leshkov, Y.; Shao-Horn, Y. Tuning Redox Transitions via Inductive Effect in Metal Oxides and Complexes, and Implications in Oxygen Electrocatalysis. *Joule* **2018**, *2* (2), 225–244.
- (4) Wei, C.; Rao, R. R.; Peng, J.; Huang, B.; Stephens, I. E. L.; Risch, M.; Xu, Z. J.; Shao-Horn, Y. Recommended Practices and Benchmark Activity for Hydrogen and Oxygen Electrocatalysis in Water Splitting and Fuel Cells. *Adv. Mater.* **2019**, *31* (31), No. 1806296.
- (5) Rao, R. R.; Huang, B.; Katayama, Y.; Hwang, J.; Kawaguchi, T.; Lunger, J. R.; Peng, J.; Zhang, Y.; Morinaga, A.; Zhou, H.; You, H.; Shao-Horn, Y. PH-and Cation-Dependent Water Oxidation on Rutile RuO₂(110). *J. Phys. Chem. C* **2021**, *125* (15), 8195–8207.
- (6) Rao, R. R.; Kolb, M. J.; Giordano, L.; Pedersen, A. F.; Katayama, Y.; Hwang, J.; Mehta, A.; You, H.; Lunger, J. R.; Zhou, H.; Halck, N. B.; Vegge, T.; Chorkendorff, I.; Stephens, I. E. L.; Shao-Horn, Y. Operando Identification of Site-Dependent Water Oxidation Activity on Ruthenium Dioxide Single-Crystal Surfaces. *Nat. Catal.* **2020**, *3* (6), 516–525.
- (7) Kwon, S.; Stoerzinger, K. A.; Rao, R.; Qiao, L.; Goddard, W. A. III; Shao-Horn, Y. Facet-Dependent Oxygen Evolution Reaction Activity of IrO₂ from Quantum Mechanics and Experiments. *J. Am. Chem. Soc.* **2024**, *146*, 11719–11725.
- (8) Rao, R. R.; Kolb, M. J.; Halck, N. B.; Pedersen, A. F.; Mehta, A.; You, H.; Stoerzinger, K. A.; Feng, Z.; Hansen, H. A.; Zhou, H.; Giordano, L.; Rossmel, J.; Vegge, T.; Chorkendorff, I.; Stephens, I. E. L.; Shao-Horn, Y. Towards Identifying the Active Sites on RuO₂(110) in Catalyzing Oxygen Evolution. *Energy Environ. Sci.* **2017**, *10*, 2626–2637.
- (9) Dionigi, F.; Zhu, J.; Zeng, Z.; Merzdorf, T.; Sarodnik, H.; Gliuch, M.; Pan, L.; Li, W.; Greeley, J.; Strasser, P. Intrinsic Electrocatalytic Activity for Oxygen Evolution of Crystalline 3d-Transition Metal Layered Double Hydroxides. *Angew. Chem.* **2021**, *133* (26), 14567–14578.
- (10) Görlin, M.; Ferreira de Araújo, J.; Schmies, H.; Bernsmeier, D.; Dresp, S.; Gliuch, M.; Jusys, Z.; Chernev, P.; Kraehnert, R.; Dau, H.; Strasser, P. Tracking Catalyst Redox States and Reaction Dynamics in Ni-Fe Oxyhydroxide Oxygen Evolution Reaction Electrocatalysts: The Role of Catalyst Support and Electrolyte PH. *J. Am. Chem. Soc.* **2017**, *139* (5), 2070–2082.
- (11) Ou, Y.; Twhight, L. P.; Samanta, B.; Liu, L.; Biswas, S.; Fehrs, J. L.; Sagui, N. A.; Villalobos, J.; Morales-Santelices, J.; Antipin, D.; Risch, M.; Toroker, M. C.; Boettcher, S. W. Cooperative Fe Sites on Transition Metal (Oxy) Hydroxides Drive High Oxygen Evolution Activity in Base. *J. Phys. Chem. C* **2023**, *14*, 7688.
- (12) Swierk, J. R.; Klaus, S.; Trotochaud, L.; Bell, A. T.; Tilley, T. D. Electrochemical Study of the Energetics of the Oxygen Evolution Reaction at Nickel Iron (Oxy)Hydroxide Catalysts. *J. Phys. Chem. C* **2015**, *119*, 19022–19029.
- (13) Grimaud, A.; Diaz-Morales, O.; Han, B.; Hong, W. T.; Lee, Y. L.; Giordano, L.; Stoerzinger, K. A.; Koper, M. T. M.; Shao-Horn, Y. Activating Lattice Oxygen Redox Reactions in Metal Oxides to Catalyze Oxygen Evolution. *Nat. Chem.* **2017**, *9* (5), 457–465.
- (14) Grimaud, A.; May, K. J.; Carlton, C. E.; Lee, Y. L.; Risch, M.; Hong, W. T.; Zhou, J.; Shao-Horn, Y. Double Perovskites as a Family of Highly Active Catalysts for Oxygen Evolution in Alkaline Solution. *Nat. Commun.* **2013**, *4* (1), 2439.
- (15) Dickens, C. F.; Montoya, J. H.; Kulkarni, A. R.; Bajdich, M.; Nørskov, J. K. An Electronic Structure Descriptor for Oxygen Reactivity at Metal and Metal-Oxide Surfaces. *Surf. Sci.* **2019**, *681*, 122–129.
- (16) Xu, Z.; Kitchin, J. R. Relating the electronic structure and reactivity of the 3d transition metal monoxide surfaces. *Cat. Comm.* **2014**, *52*, 60–64.
- (17) Kuznetsov, D. A.; Peng, J.; Giordano, L.; Román-Leshkov, Y.; Shao-Horn, Y. Bismuth Substituted Strontium Cobalt Perovskites for Catalyzing Oxygen Evolution. *J. Phys. Chem. C* **2020**, *124* (12), 6562–6570.
- (18) Burke, M. S.; Kast, M. G.; Trotochaud, L.; Smith, A. M.; Boettcher, S. W. Cobalt-Iron (Oxy)Hydroxide Oxygen Evolution Electrocatalysts: The Role of Structure and Composition on Activity, Stability, and Mechanism. *J. Am. Chem. Soc.* **2015**, *137* (10), 3638–3648.
- (19) Stevens, M. B.; Trang, C. D. M.; Enman, L. J.; Deng, J.; Boettcher, S. W. Reactive Fe-Sites in Ni/Fe (Oxy)Hydroxide Are Responsible for Exceptional Oxygen Electrocatalysis Activity. *J. Am. Chem. Soc.* **2017**, *139* (33), 11361–11364.
- (20) Trotochaud, L.; Young, S. L.; Ranney, J. K.; Boettcher, S. W. Nickel-Iron Oxyhydroxide Oxygen-Evolution Electrocatalysts: The Role of Intentional and Incidental Iron Incorporation. *J. Am. Chem. Soc.* **2014**, *136* (18), 6744–6753.
- (21) Louie, M. W.; Bell, A. T. An Investigation of Thin-Film Ni-Fe Oxide Catalysts for the Electrochemical Evolution of Oxygen. *J. Am. Chem. Soc.* **2013**, *135* (33), 12329–12337.
- (22) Friebel, D.; Louie, M. W.; Bajdich, M.; Sanwald, K. E.; Cai, Y.; Wise, A. M.; Cheng, M. J.; Sokaras, D.; Weng, T. C.; Alonso-Mori, R.; Davis, R. C.; Bargar, J. R.; Nørskov, J. K.; Nilsson, A.; Bell, A. T. Identification of Highly Active Fe Sites in (Ni,Fe)OOH for Electrocatalytic Water Splitting. *J. Am. Chem. Soc.* **2015**, *137* (3), 1305–1313.
- (23) Yuan, S.; Peng, J.; Cai, B.; Huang, Z.; Garcia-Esparza, A. T.; Sokaras, D.; Zhang, Y.; Giordano, L.; Akkiraju, K.; Zhu, Y. G.; Hübner, R.; Zou, X.; Román-Leshkov, Y.; Shao-Horn, Y. Tunable Metal Hydroxide–Organic Frameworks for Catalysing Oxygen Evolution. *Nat. Mater.* **2022**, *21* (6), 673–680.
- (24) Zheng, D. J.; Görlin, M.; McCormack, K.; Kim, J.; Peng, J.; Xu, H.; Ma, X.; LeBeau, J. M.; Fischer, R. A.; Román-Leshkov, Y.; Shao-Horn, Y. Linker-Dependent Stability of Metal-Hydroxide Organic Frameworks for Oxygen Evolution. *Chem. Mater.* **2023**, *35* (13), 5017–5031.
- (25) Scott, S. B.; Rao, R. R.; Moon, C.; Sørensen, J. E.; Kibsgaard, J.; Shao-Horn, Y.; Chorkendorff, I. The Low Overpotential Regime of Acidic Water Oxidation Part I: The Importance of O₂ Detection. *Energy Environ. Sci.* **2022**, *15*, 1977–1987.
- (26) Abed, J.; Kim, J.; Shuaibi, M.; Wander, B.; Duijff, B.; Mahesh, S. Open Catalyst Experiments 2024 (OCx24): Bridging Experiments and Computational Models. *arXiv* **2024**, *2024*, 1–38.
- (27) Tran, R.; Lan, J.; Shuaibi, M.; Wood, B. M.; Goyal, S.; Das, A.; Heras-domingo, J.; Kolluru, A.; Rizvi, A.; Shoghi, N.; Sriram, A.; Therrien, F.; Abed, J.; Voznyy, O.; Sargent, E. H.; Ulissi, Z.; Zitnick, C. L. The Open Catalyst 2022 (OC22) Dataset and Challenges for Oxide Electrocatalysts. *ACS Catal.* **2023**, *13*, 3066–2084.
- (28) Xie, T.; Grossman, J. C. Crystal Graph Convolutional Neural Networks for an Accurate and Interpretable Prediction of Material Properties. *Phys. Rev. Lett.* **2018**, *120* (14), No. 145301.
- (29) Zeni, C.; Pinsler, R.; Zügner, D.; Fowler, R.; Horton, M.; Fu, X.; Shysheya, S.; Crabbé, J.; Sun, L.; Smith, J.; Tomioka, R.; Xie, T. MatterGen: A Generative Model for Inorganic Materials Design. *arXiv* **2023**, 1–56.
- (30) Ulissi, Z. W.; Singh, A. R.; Tsai, C.; Nørskov, J. K. Automated Discovery and Construction of Surface Phase Diagrams Using Machine Learning. *J. Phys. Chem. Lett.* **2016**, *7* (19), 3931–3935.
- (31) Torelli, D. A.; Francis, S. A.; Crompton, J. C.; Javier, A.; Thompson, J. R.; Brunschwigg, B. S.; Soriaga, M. P.; Lewis, N. S. Nickel-Gallium-Catalyzed Electrochemical Reduction of CO₂ to Highly Reduced Products at Low Overpotentials. *ACS Catal.* **2016**, *6* (3), 2100–2104.
- (32) Clausen, C. M.; Nielsen, M. L. S.; Pedersen, J. K.; Rossmel, J. Ab Initio to Activity: Machine Learning-Assisted Optimization of

High-Entropy Alloy Catalytic Activity. *High Entropy Alloy. Mater.* **2023**, *1* (1), 120–133.

(33) Lunger, J. R.; Karaguesian, J.; Chun, H.; Peng, J.; Tseo, Y.; Shan, C. H.; Han, B.; Shao-Horn, Y.; Gómez-Bombarelli, R. Towards Atom-Level Understanding of Metal Oxide Catalysts for the Oxygen Evolution Reaction with Machine Learning. *npj Comput. Mater.* **2024**, *10* (1), 80.

(34) Reddington, E.; Sapienza, A.; Gurau, B.; Viswanathan, R.; Sarangapani, S.; Smotkin, E. S.; Mallouk, T. E.; Haber, J. A.; Lewis, N. S. Combinatorial Electrochemistry: A Highly Parallel, Optical Screening Method for Discovery of Better Electrocatalysts. *Chemtracts* **1999**, *12* (5), 319–321.

(35) Gerken, J. B.; Chen, J. Y. C.; Massé, R. C.; Powell, A. B.; Stahl, S. S. Development of an O₂-Sensitive Fluorescence-Quenching Assay for the Combinatorial Discovery of Electrocatalysts for Water Oxidation. *Angew. Chemie - Int. Ed.* **2012**, *51* (27), 6676–6680.

(36) Gerken, J. B.; Shaner, S. E.; Massé, R. C.; Porubsky, N. J.; Stahl, S. S. A Survey of Diverse Earth Abundant Oxygen Evolution Electrocatalysts Showing Enhanced Activity from Ni-Fe Oxides Containing a Third Metal. *Energy Environ. Sci.* **2014**, *7* (7), 2376–2382.

(37) Dogan, C.; Stöwe, K.; Maier, W. F. Optical High-Throughput Screening for Activity and Electrochemical Stability of Oxygen Reducing Electrode Catalysts for Fuel Cell Applications. *ACS Comb. Sci.* **2015**, *17* (3), 164–175.

(38) Welsch, F. G.; Stöwe, K.; Maier, W. F. Rapid Optical Screening Technology for Direct Methanol Fuel Cell (DMFC) Anode and Related Electrocatalysts. *Catal. Today* **2011**, *159* (1), 108–119.

(39) Welsch, F. G.; Stöwe, K.; Maier, W. F. Fluorescence-Based High Throughput Screening for Noble Metal-Free and Platinum-Poor Anode Catalysts for the Direct Methanol Fuel Cell. *ACS Comb. Sci.* **2011**, *13* (5), 518–529.

(40) Lohrengel, M. M.; Moehring, A.; Pilaski, M. Electrochemical Surface Analysis with the Scanning Droplet Cell. *Fresenius. J. Anal. Chem.* **2000**, *367* (4), 334–339.

(41) Gregoire, J. M.; Xiang, C.; Liu, X.; Marcin, M.; Jin, J. Scanning Droplet Cell for High Throughput Electrochemical and Photoelectrochemical Measurements. *Rev. Sci. Instrum.* **2013**, *84* (2), No. 024102.

(42) Deshpande, K.; Mukasyan, A.; Varma, A. High Throughput Evaluation of Perovskite-Based Anode Catalysts for Direct Methanol Fuel Cells. *J. Power Sources* **2006**, *158* (1), 60–68.

(43) Green, M. L.; Takeuchi, I.; Hatrick-Simpers, J. R. Applications of High Throughput (Combinatorial) Methodologies to Electronic, Magnetic, Optical, and Energy-Related Materials. *J. Appl. Phys.* **2013**, *113* (23), No. 231101.

(44) Koinuma, H.; Takeuchi, I. Combinatorial Solid-State Chemistry of Inorganic Materials. *Nat. Mater.* **2004**, *3* (7), 429–438.

(45) Peng, J.; Damewood, J.; Gómez-Bombarelli, R. Data-Driven Physics-Informed Descriptors of Cation Ordering in Multicomponent Perovskite Oxides. *Cell Rep. Phys. Sci.* **2024**, *5* (5), No. 101942.

(46) Takeuchi, I.; Chang, H.; Gao, C.; Schultz, P. G.; Xiang, X. D.; Sharma, R. P.; Downes, M. J.; Venkatesan, T. Combinatorial Synthesis and Evaluation of Epitaxial Ferroelectric Device Libraries. *Appl. Phys. Lett.* **1998**, *73* (7), 894–896.

(47) Chen, Z.; Kim, C. H.; Thompson, L. T.; Schneider, W. F. LDA +U Evaluation of the Stability of Low-Index Facets of LaCoO₃ Perovskite. *Surf. Sci.* **2014**, *619*, 71–76.

(48) Tatara, R.; Kwabi, D. G.; Batcho, T. P.; Tulodziecki, M.; Watanabe, K.; Kwon, H. M.; Thomas, M. L.; Ueno, K.; Thompson, C. V.; Dokko, K.; Shao-Horn, Y.; Watanabe, M. Oxygen Reduction Reaction in Highly Concentrated Electrolyte Solutions of Lithium Bis(Trifluoromethanesulfonyl)Amide/Dimethyl Sulfoxide. *J. Phys. Chem. C* **2017**, *121* (17), 9162–9172.

(49) Zhang, G.; Wei, Q.; Yang, X.; Tavares, A. C.; Sun, S. RRDE Experiments on Noble-Metal and Noble-Metal-Free Catalysts: Impact of Loading on the Activity and Selectivity of Oxygen Reduction Reaction in Alkaline Solution. *Appl. Catal. B Environ.* **2017**, *206*, 115–126.

(50) Bonakdarpour, A.; Lefevre, M.; Yang, R.; Jaouen, F.; Dahn, T.; Dodelet, J. P.; Dahn, J. R. Impact of Loading in RRDE Experiments on Fe-N-C Catalysts: Two- or Four-Electron Oxygen Reduction? *Electrochem. Solid-State Lett.* **2008**, *11* (6), B105–B108.

(51) Lee, C.; Kwak, J.; Anson, F. C. Application of Scanning Electrochemical Microscopy to Generation/Collection Experiments with High Collection Efficiency. *Anal. Chem.* **1991**, *63* (2), 1501.

(52) Wang, Z.; Tan, S.; Xiong, Y.; Wei, J. Effect of B Sites on the Catalytic Activities for Perovskite Oxides La_{0.6}Sr_{0.4}CoxFe_{1-x}O_{3-δ} as Metal-Air Batteries Catalysts. *Prog. Nat. Sci. Mater. Int.* **2018**, *28* (4), 399–407.